Journal of Power Sources 416 (2019) 155–162

Contents lists available at ScienceDirect

Journal of Power Sources

journal homepage: www.elsevier.com/locate/jpowsour

Imaging of the desaturation of gas diffusion layers by synchrotron computed tomography

Logan Battrell[a], Virat Patel[b], Ning Zhu[b,c], Lifeng Zhang[b], Ryan Anderson[a,*]

[a] Department of Chemical and Biological Engineering, Montana State University, Bozeman, MT, 59717, USA
[b] Department of Chemical and Biological Engineering, University of Saskatchewan, Saskatoon, SK, S7N 5A9, Canada
[c] Canadian Light Source, Saskatoon, SK, S7N 2V3, Canada

HIGHLIGHTS

- Spatial and temporal GDL saturation is analyzed from Synchrotron X-ray CT data.
- As the GDL is segmented spatially, variations in the desaturation rate are noted.
- Overall desaturation rate of 0.0030 ± 0.0013 $\mu L\,cm^{-2}\,s^{-1}$ is spatially investigated.
- Spatially and temporally resolved desaturation rates are key to model validation.

ARTICLE INFO

Keywords:
Gas diffusion layer
Saturation
X-ray radiography
4-D imaging
PEM fuel cell
Water management

ABSTRACT

The 4-D imaging and quantification of the desaturation of an initially flooded gas diffusion layer (GDL) with a serpentine gas flow channel by synchrotron radiography is presented. An imaging area with a diameter of 10 mm allows for the study of how the natural anisotropy of a GDL affects the desaturation profile. The GDL is progressively spatially segmented from the overall domain down to sections of the individual channels and ribs. Temporal saturation profiles and desaturation rates are presented for each step of this progressive segmentation. Although the desaturation of the overall domain initially appears to be a constant and steady process with a desaturation rate of 0.0030 $\mu L\,cm^{-2}\,s^{-1}$, segmented results display heterogeneous behavior with over two-fold differences between areas of the flow field. Segmented saturation surface plots are presented that spatially show how this heterogeneity occurs within the entire domain. Results indicate that initial conditions, anisotropic material properties, and flow field geometry all play a key role in determining local desaturation behavior. The larger domain considered here provides valuable data for future modeling studies that combine continuum studies of flow in the gas flow channels with GDL pore network models that consider two-phase flow behavior.

1. Introduction

The Gas Diffusion Layer (GDL) is a key component within the Membrane Electrode Assembly (MEA) of Polymer Electrolyte Membrane (PEM) fuel cells. These hydrogen fuel cells have been the focus of research due to their demonstrated potential as scalable energy conversion devices that feature zero local emissions, high power density, and rapid start-up [1]. The GDL is a thin porous layer that is located between the catalyst layer and the gas flow channels within both the anode and cathode. Here, thin refers to a porous media where the layer thickness is of a similar magnitude to a typical pore diameter (L_{GDL} = 100–300 μm, $D_{GDL\text{-}Pore}$ = 1–100 μm) [2]. This thin property introduces problems in studying this layer, since accurate modeling dictates that the domain length should be 10–15 times larger than the average pore size, rather than the one order of magnitude or less difference commonly found in GDLs [3,4]. Briefly, the GDL is responsible for promoting transport of the reactive species to the catalytic sites, facilitating the removal of product water from the cathode catalyst layer, and conducting electrons with low resistance. Key to its functionality is the proper management of the overall water saturation, specifically maintaining enough water to hydrate the polymer membrane, while not accumulating water to the point where the GDL is considered flooded, wherein gas transport to the catalyst layer is restricted or completely blocked [5,6]. Poor water management can lead to material degradation, lowered cell performance, and in extreme cases, total cell failure [7,8].

* Corresponding author.
E-mail address: ryan.anderson@montana.edu (R. Anderson).

https://doi.org/10.1016/j.jpowsour.2019.01.089
Received 5 October 2018; Received in revised form 19 December 2018; Accepted 28 January 2019
Available online 07 February 2019
0378-7753/

This critical layer has been reviewed in detail, discussing the various materials, properties, characteristics, and varying structures [2,7,9]. As proficient water management is clearly key to efficient fuel cell operation, numerous approaches have been developed and investigated to address this challenge. These include preventative measures to keep the GDL from ever reaching this flooded state and reactive strategies that desaturate the GDL once it has been identified as heading towards the flooded state. Several groups have studied a variety of material modifications to enhance or better understand water management. These investigations include introducing perforations to the cathode microporous layer (MPL) [10], varying the MPL composition based on the operating conditions of the cell [11], varying the hydrophobicity and structure of various cathode layers to optimize electrochemical performance of the cell [12], and utilizing a double layered GDL with a hydrophobicity gradient [13]. Additionally, new materials and architectures have been investigated to determine if they could potentially replace traditional layers. This includes replacing the cathode bipolar plate with a hydrophilic water transport plate [14], the investigation of novel electrospun GDLs and their effect on water management [15], as well as numerous studies into various flow fields designed to promote water removal, previously reviewed [16]. Many reactive strategies rely on some sort of signal analysis combined with an operational change to reduce or remove performance losses [17]. All of these net water management strategies are in effect governed by the pore scale water dynamics occurring within the GDL. For example, a proposed dynamic intermittent humidification scheme that evaporates excess water based on voltage monitoring functions by removing excess water both convectively and through evaporation [18]. Additionally, an air flow control system was designed to regulate the overall water content within the cell, based on a model that controls the humidification of the air stream [19]. Finally, a diagnostic technique was developed to quantify the desaturation of a flooded cathode based on an analysis of the anode pressure drop and the introduction of a dry anode stream [20]. As the pore-scale behavior is difficult to quantify, these control schemes are empirical and often specific to a cell's geometry or operating condition. In order to better understand the basic transport phenomena and governing properties, recent work has focused on numerical modeling and experimental visualization at the pore scale, which has the potential to allow for intelligent material design and better informed control schemes.

Various modeling strategies have been implemented to try to better understand water accumulation and transport within the GDL. Recent reviews of both performance and transport models was provided by Wu [21] and of cell-scale multiphase flow modeling by Andersson et al. [22]. As mentioned, one of the distinguishing factors of a GDL when compared to other porous materials is the fact that its pore size is on the same scale as the overall thickness of the layer. A recent investigation by García-Salaberri et al. [23] showed that a representative element volume for a GDL could not be identified in the through-plane due to its relative thinness in relation to the average pore size. One approach that has expanded is pore network models (PNM). Through PNMs, researchers have been able to represent the GDL as a network of interconnected throats and pores and have simulated two-phase flow. Recently, Aghighi and Gostick [24] created a PNM to predict phase changes and capture local water distributions with a constant voltage boundary under different operating conditions. Similarly, Belgacem et al. [25] created a coupled continuum and condensation PNM to investigate water accumulation in a PNM when coupled with the electrochemical phenomena occurring at the catalyst layer. Additionally, Medici et al. [26] utilized a coupled continuum-PNM model to understand how stacking anode GDLs increased performance. X-ray computed tomography (X-ray CT) was used to extract GDL properties, used as inputs for the model. Due to computational requirements, all of these models have limited their unit geometry to be roughly the width of one channel and rib. However, as computational capabilities expand, the need for larger domain data sets will be key in potentially validating results or seeding initial conditions. Since the GDL presents a unique case, experimental data is necessary to help validate the development of new models and inform new material designs.

To address these needs, the visualization of both the saturation and desaturation of this critical layer has been a research focus in recent years. Synchrotron radiography is a key technique to measure water in PEM fuel cells, due to its sufficient phase contrast and high temporal and spatial resolution, allowing for the visualization and quantification of water content within the various layers of the MEA [27]. Synchrotron radiography has been used by Kruger et al. [28] to visualize the increasing cathode GDL saturation as the current density of the cell is increased, by Lee et al. [29] to investigate the effect of MPL thickness on GDL water saturation, and by Arlt et al. [30] to investigate the effect of aging on GDL water management capabilities. Muirhead et al. [31] quantified the relation between liquid water saturation and oxygen transport resistance and found that existing correlations relating porosity and saturation to diffusivity could be improved by GDL-specific tuning. The majority of these studies were 2-D investigations in the in-plane of the fuel cell, likely due to the limiting nature of the components necessary for an operating fuel cell, specifically the metallic and graphite components, both of which have high absorptivity. X-ray CT is a specific visualization tool that has also been used to investigate different aspects of the desaturation of a GDL. Recently, Lal et al. [32] used a laboratory CT scanner to take images of a 1 mm × 1 mm region of a GDL with a single channel to determine the effect of temperature on the GDL evaporation rate. Zenyuk et al. [33] used synchrotron X-ray CT to take measurements of a 3.8 mm diameter GDL sample with a single gas channel and determined the effect that GDL saturation had on the evaporation rate.

In summary, the visualization of water accumulation and desaturation within the GDL is a topic that has received recent attention. Although many groups have examined this effect in 2-D with an active cell or in 3-D with a single channel, the research of desaturation of a full GDL domain in 3-D with a typical fuel cell flow field geometry is something that has not thoroughly been investigated. Recently, synchrotron X-ray CT was used by Battrell et al. [34] to investigate the transient desaturation process to separate the relative contributions of evaporation and convection to the overall GDL desaturation process of a 10 mm diameter sample, by a 5 channel serpentine gas flow channel. The present work expands on this previous study by further investigating and quantifying the spatial gradients present within the GDL over time. This 4-D information is valuable to the modeling community, which could use this data to validate and confirm theoretical models. These results can also inform future GDL designs, which may be able to better intrinsically assist in the overall water management of the fuel cell. Saturation gradients are broken down from overall desaturation profiles, to rib and channel, down to individual ribs and channels, and finally the segmentation of each rib and channel, allowing for a more detailed spatial and temporal investigation of the desaturation of this thin porous media.

2. Methods

The protocols used for this study were discussed in detail previously [34], and are presented briefly here for reference, as well as to highlight improvements made in order to facilitate further data analysis.

2.1. Desaturation protocol

The protocol for the desaturation of the GDL sample was the same used in the previous study [34] and is briefly reviewed here. The GDL sample was initially saturated by being submersed in a water bath and agitated for 1 min. The GDL was then placed within the acrylic test cell, seen in Fig. 1-A, which was then closed and tightened until water could be seen within the gas channels on top of the GDL. After taking a stop-and-shoot (S + S) CT scan to establish initial saturation, dry air at room

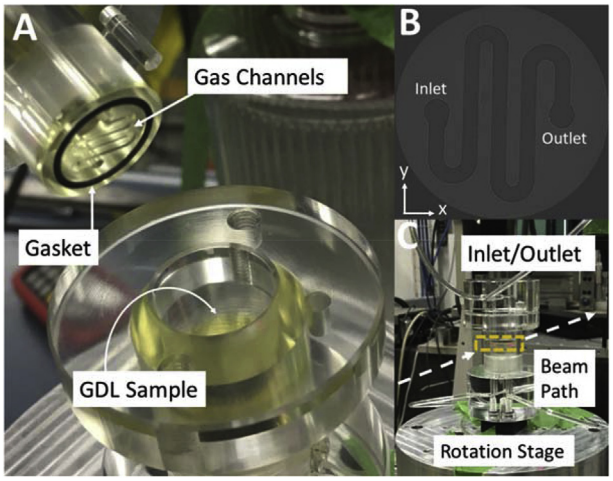

Fig. 1. A) Disassembled cell displaying gas channels, gasket, and where the GDL is placed in the bottom piece, B) X-ray image of gas flow field with labeled inlet and outlet, and C) assembled flow cell in beam setup, with the imaging area highlighted in yellow. (For interpretation of the references to colour in this figure legend, the reader is referred to the Web version of this article.)

temperature (22 °C) was introduced at a flowrate of 50 N ml min^{-1}, corresponding to the required flowrate to operate a fuel cell at 1000 mA cm^{-2} at a stoichiometric point of 2. On-the-fly (OTF) scans were then collected every minute, a rate that was based on the computational limits of the image acquisition computer, for the first 30 min of the experiment, and then every 5 min. Data collection was reduced at this later period due to memory requirements, and because the most dynamic transient behavior occurred early on in the test.

2.2. Sample description and flow cell design

The focus of the study was on the 35 AA GDL from Sigracet. Although a GDL without any hydrophobic treatment is not traditionally used in PEM fuel cell applications, this GDL is the substrate from which the 35 BA (5% PTFE) and 35 BC (5% PTFE and MPL) GDLs are made from. These GDLs were not investigated because previous results showed that the BA GDL fully desaturates in this setup in roughly 2.5 min [34], making the spatial gradients and transient desaturation much harder to visualize and quantify. Since the AA GDL is able to initially saturate to a much higher percentage, and the overall desaturation rate is roughly four times slower, capturing the intermediate saturation profiles at sufficient temporal resolution was made possible by selecting this material instead. The acrylic test cell used for this study had the same overall specifications as the one used previously, with a small change to the gas channel geometry that allowed for the increase of the overall channel length to 39.1 mm. Specifically, the gas channel, seen in Fig. 1-B, was 1 mm (w) x 0.5 mm (d), the first and last ribs had a width of 1.2 mm, and the middle two ribs had a width of 0.8 mm.

2.3. Synchrotron setup/parameters

All of the imaging experiments for this study were performed at the 3rd generation synchrotron facility Canadian Light Source Inc. (CLS) (Saskatoon, Canada) at the BioMedical Imaging and Therapy (BMIT) 05B1-1 beamline [35]. All beam parameters, including the high intensity white beam (polychromatic beam), sample to detector distance (50 cm), detector (Hamamatsu AA40) and camera (Hamamatsu ORCA Flash 4.0) were the same as used in the previous study [34]. This setup allowed for two CT scan modes, a sub 10 s OTF scan mode, consisting of 1500 projections, and a high-quality S + S scan mode, consisting of 2250 projections, both with pixel sizes of 6.4 μm. For the OTF protocol, CT scans could be consecutively conducted every minute, and the data acquisition time was currently limited by the mechanical capacity of the rotation stage and the processing time of the imaging computer. Fig. 1-C shows the acrylic test cell on the rotation stage, highlighting both the imaging area and beam path.

2.4. Image processing and GDL spatial analysis

Background correction was performed with ImageJ [36], using dark-field and flat-field images to correct for any artifacts that might have been introduced by the monochromator, filter, or detector. The 3-D reconstruction was then performed with NRecon 1.7.1.0 (Bruker). These full CT images were then loaded into MetaMorph (Molecular Devices LLC) for post-reconstruction analysis, specifically segmentation

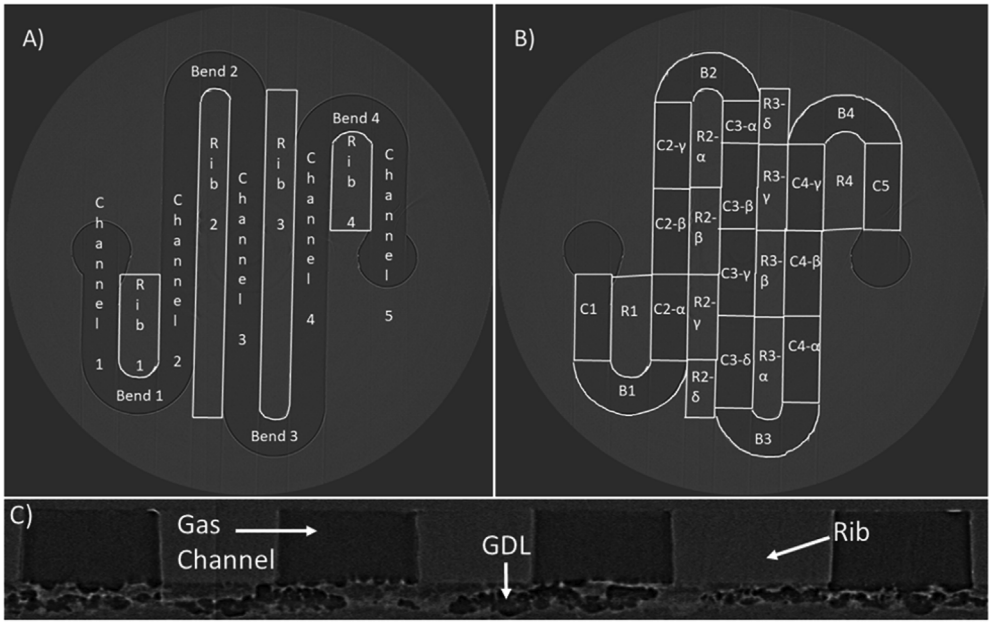

Fig. 2. A) Schematic showing the naming convention for individual channels and ribs and B) the full segmentation geometry and further naming conventions (C = channel, R = rib, B = bend) used for subsequent data analysis, C) 2-D slice image showing GDL, Gas channels, and Ribs.

and quantification. For this study, the GDL was progressively segmented into smaller and smaller regions in order to separate spatial saturation gradients from the overall desaturation profile. These different segmentation orientations and the naming conventions used throughout the rest of the paper can be seen in Fig. 2. In all cases, the saturation represents the liquid volume in the various domains, e.g. the entire GDL or channel 1. The transient desaturation rates are calculated by considering the difference in saturation every five minutes, normalized by the cross sectional area in the through plane of the segment being analyzed. This approach reduces the noise associated with analysis every minute and is consistent with the time-steps at the end of the trial. Thus, eight rates are presented for the 40 min of collected data.

3. Results

The temporal saturation profiles and transient desaturation rates are examined as the domain is segmented down from the overall domain, to channels and ribs, then to the individual channels and ribs, and finally to the spatially segmented saturation profile. This section focuses on the specific results of this study, while the discussion section focuses on comparisons to other published studies, including published desaturation rates and pore network models.

3.1. Desaturation quantification of the entire GDL sample

The first analysis was to consider the overall desaturation of the entire GDL domain, presented as the temporal saturation profile and transient desaturation rates in Fig. 3. Based on the initial saturation, time to fully desaturate, and the volume of the domain, the overall desaturation rate is calculated to be 0.0030 $\mu L\,cm^{-2}\,s^{-1}$. From this figure, it is seen that the overall GDL desaturation has two approximately linear regions, with the transition between them happening between the 15 and 20 min mark, which corresponds with a step-change in the desaturation rate from 0.0018 ± 0.0002 $\mu L\,cm^{-2}\,s^{-1}$ to 0.0042 ± 0.0004 $\mu L\,cm^{-2}\,s^{-1}$.

3.2. Desaturation quantification: channels vs. ribs

The next step in the analysis of the desaturation profile was to isolate the channel and rib saturation from overall profile. The channel domain is comprised of the four bends and channels 1–5, while the rib domain is the average of ribs 1–4, as specified in Fig. 2-A. It is key to point out that in this segmentation some of the outer area that was previously included in the overall analysis was cropped out to only include rib directly located next to two channels. In Fig. 4, the temporal

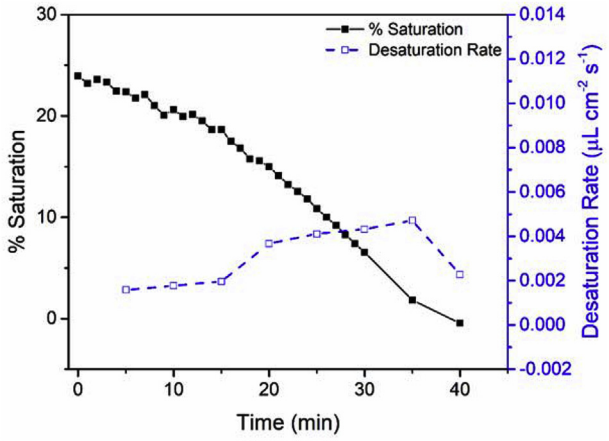

Fig. 3. Temporal saturation profile and transient desaturation rate for the overall GDL domain. For reference, the desaturation rate is calculated as a 5 min average.

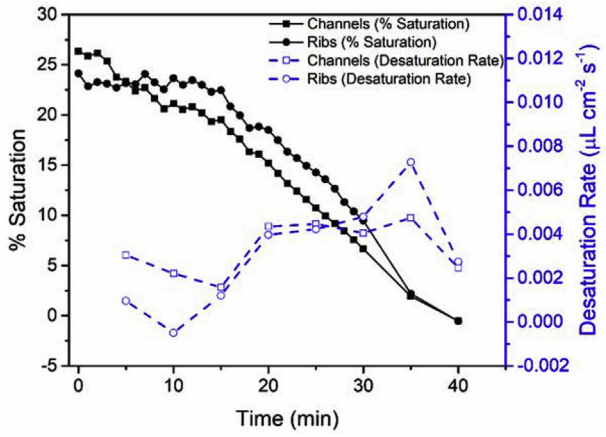

Fig. 4. Temporal saturation profile and transient desaturation rate for both the channel and rib domains.

saturation profiles and transient desaturation rates are presented for both the channel and rib domains. At this stage of segmentation, the overall desaturation rates for both the channel and rib domains are calculated to be similar to that of the overall GDL, 0.0034 ± 0.0012 $\mu L\,cm^{-2}\,s^{-1}$ and 0.0031 ± 0.0025 $\mu L\,cm^{-2}\,s^{-1}$ respectively. Interestingly, the temporal saturation profile underneath the channels is very similar to the overall GDL temporal saturation profile, seen in Fig. 3. Comparing these two saturation profiles to the profile underneath the ribs, an interesting difference is found. The saturation underneath the ribs is seen to remain mostly constant or increase, as denoted by the negative desaturation rate, until the 15–16 min mark, when the ribs begin to have a similar desaturation rate to that seen in the channels. This overlap of desaturation rates ends starting around the 30 min mark, when the ribs undergo rapid desaturation.

Next, the individual channels and ribs were separated to investigate if there was a spatial saturation difference from inlet to outlet across the GDL. The reader is referred back to Fig. 2-A to reference the naming convention for the individual ribs and channels in the cell. Fig. 5 displays the temporal saturation profiles and desaturation rates for each rib and gas flow channel. From Fig. 5-A, it is seen that there is a high level of heterogeneity between each of the channels. Looking at the transient desaturation rates in Fig. 5-C, it is seen that all of the channels have unique desaturation profiles, with peak desaturation rates occurring at different time points throughout the experiment. While it makes sense that channel one is the first to peak at the beginning of the experiment, as it is located directly next to the inlet, the next peak occurs under channel 5 from 15 to 20 min, which is located next to the outlet. The final peak occurs in the middle of the overall GDL domain under channel 3 from 30 to 35 min. Also interesting is that for the first 15 min, the desaturation rate underneath channel 2 and 3 is close to zero. Looking to the results underneath the ribs, the same extent of heterogeneity is not observed. First, all four ribs display a lag time before significant desaturation occurs, generally between the 12 and 16 min mark. However, it is seen that in rib 3 the saturation actually slightly increases from the 4–12 min mark. It is also underneath rib 3 that the highest overall desaturation rate is observed from the 30 min mark until the end of the test.

These segmented temporal saturation profiles and transient desaturation rates demonstrate the large scale of heterogeneity present throughout the entire GDL during the overall desaturation process. This is in stark contrast to the investigation of the overall domain, where the process was seen to be mostly steady and consistent.

3.3. Desaturation quantification: channel and rib segmentation

Next, the individual channels and ribs were segmented, with

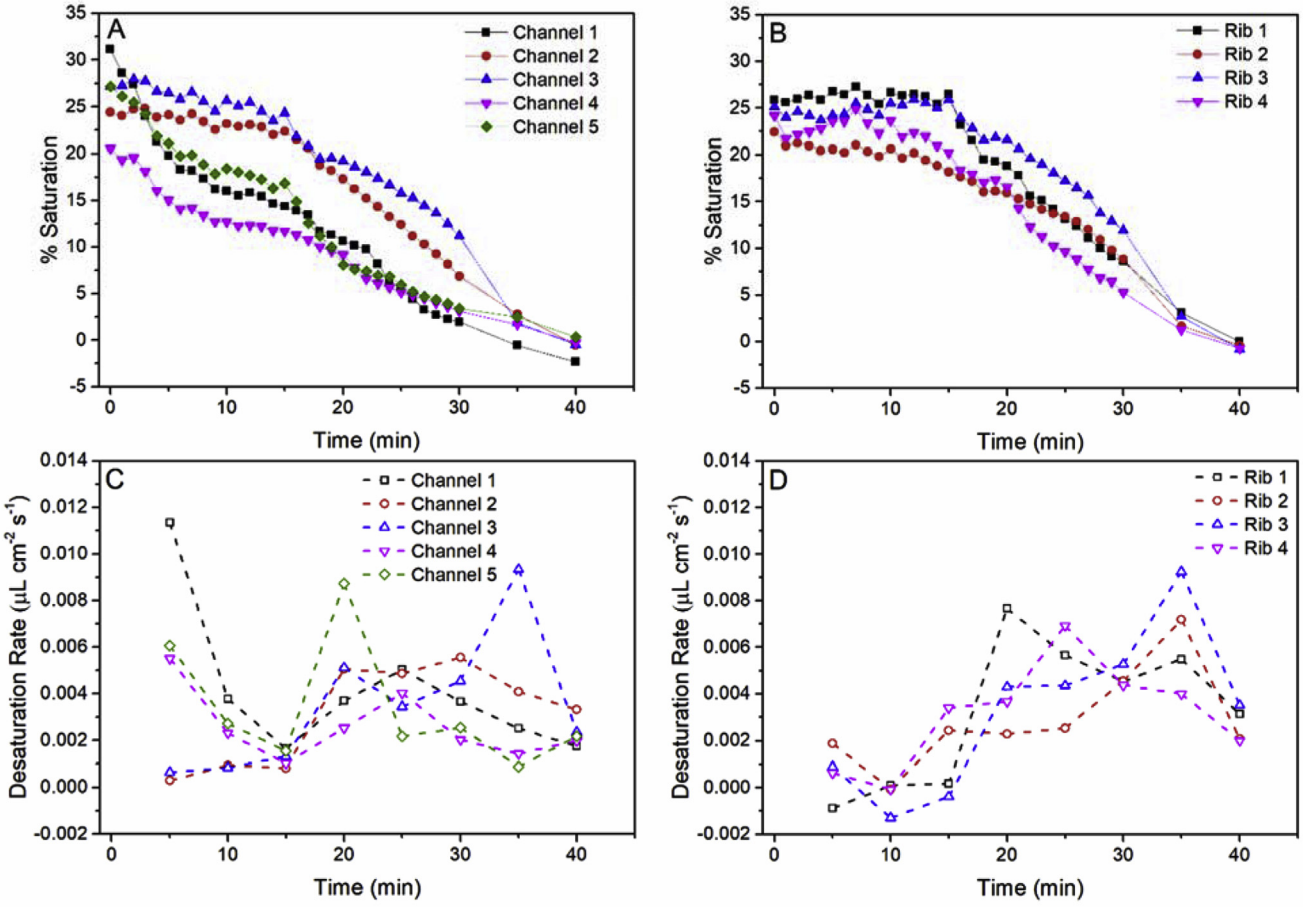

Fig. 5. Temporal saturation profiles A) underneath each individual gas flow channel, where channel 1 is the inlet and channel 5 is the outlet, and B) underneath each individual rib. Transient desaturation rates presented as 5 min averages C) for each channel and D) for each rib.

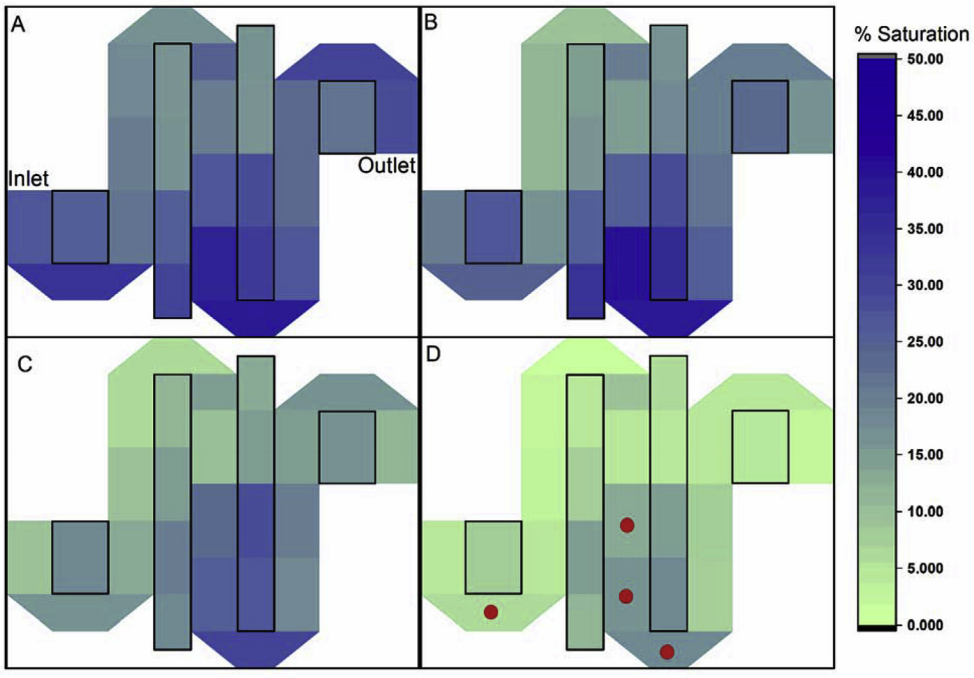

Fig. 6. Spatial saturation plots showing the segmented saturation profiles after A) 1 min of dry air flow, B) 10 min of dry airflow, C) 20 min of dry airflow, and D) 30 min of dry airflow. (Color figure online). (For interpretation of the references to colour in this figure legend, the reader is referred to the Web version of this article.)

geometries and naming conventions displayed in Fig. 2-B. The saturation measurements for each segment were translated onto a matrix based on the spatial coordinates of each segment and are presented as surface plots. This plot allows each segment to be visualized at the same spatial scale (e.g. channel width or rib width) as occurs in the actual experimental setup. Fig. 6 presents the spatial saturation plots at

selected time points throughout the desaturation process. From these selected saturation plots, it can be seen that the highest concentration of water was consistently found underneath the third bend throughout the test. Between the first and tenth minute of airflow, the saturation only slightly decreases in this location by 0.9%. Fig. 5-C shows that channels 1, 4, and 5 had the highest desaturation rates at the start of the test. Comparing Fig. 6-A and B, it is seen that the majority of the desaturation in channel 4 occurred at the end of the channel, closest to bend 4. Similarly, in channels 2 and 3 it is seen that the middle and top portions of the channel (relative to the figure) desaturate faster than the lower areas. Taken together, this shows a preference of desaturation to the upper region of the overall GDL domain. This, along with the behavior observed in bend 3, suggests that the gas flow was potentially bypassing underneath the ribs and following a more direct path from the inlet to outlet via the in-plane flow paths available in the porous GDL.

The heterogeneous nature of the desaturation is best observed by comparing Fig. 6-A and C. Specifically, it is seen that although the regions centered around bend 1 and bend 4 started at a relatively high saturation, they both underwent faster desaturation then areas with lower initial saturation, such as channel 3 and 4 and their neighboring ribs. Fig. 6-D shows that after 30 min of airflow the majority of the domain has completely desaturated, except for the region around the third bend and the neighboring sections of ribs 2 and 3. By 40 min, the entire domain is at 0% saturation.

In this approach, it is seen that both neighboring segments, as well as regions with similar geometries, display high levels of variance in their desaturation profiles. This factor is further illustrated by Fig. 7, where the temporal saturation profiles of four selected segments are presented. For reference, these four segments are marked in Fig. 6-D by red dots. Fig. 7-A displays saturation profiles of two neighboring segments in channel 3. There is initially a 7% magnitude difference between the saturation values between the two regions. From here, the saturation for both segments stays mostly constant for the first 20 min of the experiment. At this point channel 3-γ (C3- γ) undergoes rapid desaturation down to approximately the same value as seen in channel 3-δ (C3- δ). From here, the desaturation of the two segments follows a similar path until 35 min where a difference of 5.5% saturation appears. A divergence is also found between the saturation profiles of bend 1 (B1) and bend 3 (B3). While B1 almost immediately begins to desaturate, B3 briefly increases in saturation for the first 5–10 min until its constant desaturation begins, rapidly accelerating around 25 min.

These selected saturation profiles demonstrate that there is no representative or average desaturation path that can be applied between the different segments. Even between segments that have similar geometries, heterogeneous behavior is consistently observed, pointing to the impact that local material structures, such as permeability, pore size, and initial saturation have on desaturation.

4. Discussion

This section focuses on comparisons to other studies including published desaturation rates and pore network models. Potential uses for the data set as future validation and key findings are also summarized.

4.1. Analysis of overall desaturation rate

As discussed in section 3.1, the overall desaturation rate for the entire GDL domain was found to be 0.0030 μL cm^{-2} s^{-1}. While this value is lower than that reported by other recent studies, this difference can be explained by the experimental conditions used in each study. Zenyuk et al. [33] reported a value of 0.09 μL cm^{-2} s^{-1}. However, their experiment was at a flowrate of 600 N ml min^{-1}, which is an order of magnitude higher than that used in this study, 50 N ml min^{-1}, and it has been shown by previous work that there is a convective component to GDL desaturation [34]. Multiple studies [37,38] have also shown that increasing the flowrate results in an increase of the evaporation rate. Additionally, the GDL investigated in that study had PTFE treatment, which has been shown to alter both the location of saturating water as well as the rate of desaturation [34]. Similarly, Lal et al. [32] determined an evaporation rate of 0.9 μL cm^{-2} s^{-1}; however, their experiment was run at 60 °C with a gas velocity of 6 m s^{-1}, while this study was performed at 22 °C and 0.8 m s^{-1}. In addition to the effects due to a larger flowrate and PTFE treatment, an increased temperature has an exponential impact on an evaporation rate [37]. Finally, both of those studies investigated a single channel over a much smaller domain, 3.2 mm diameter in the investigation by Zenyuk et al. [33], and 1 mm × 1 mm for Lal et al. [32], compared to the 5 serpentine channels within a region of interest of 10 mm in diameter in this study. Taking all of these factors into consideration, the difference between the calculated overall desaturation rates makes qualitative sense.

4.2. Analysis of segmented results

As reviewed in section 1, the typical pore network modeling domain size is currently restricted by computational power, so most models are limited to a unit cell approximately the width of one channel and rib

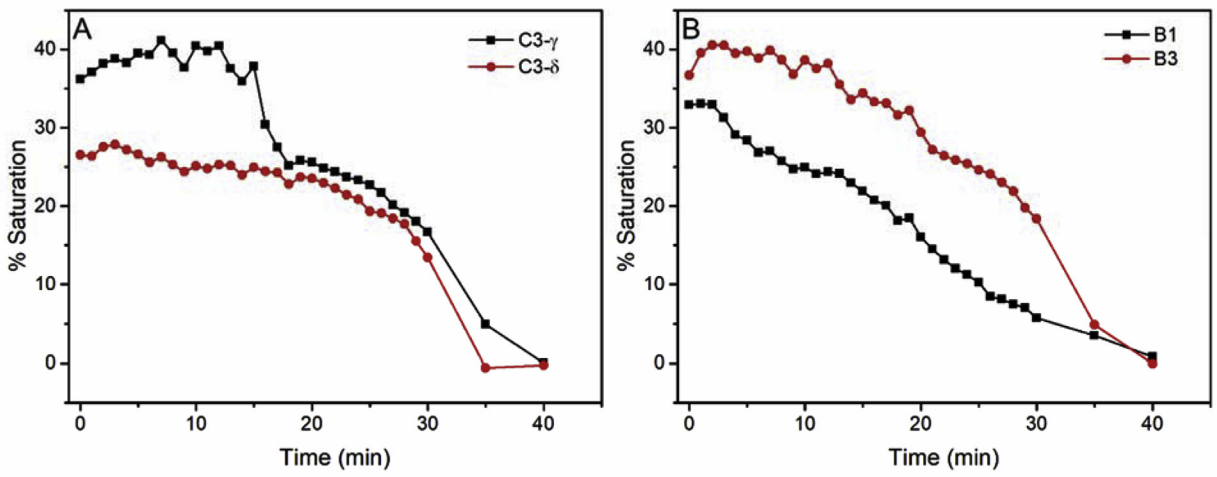

Fig. 7. Temporal saturation profiles for select segments in Fig. 6. A) Channel 3-γ and channel 3-δ and B) bend 1 and bend 3. These results indicate different rates of desaturation that are not dependent on flow field geometry or initial conditions.

(1–2 mm) [24–26]. Results from this study show that as computational capabilities expand, both initial conditions and flow field geometry will need to be taken into consideration in order to fully capture and model the transient saturation behavior. The more common flow field geometries, specifically parallel, serpentine, and interdigitated, have varying characteristics. Parallel channels feature lower pressure drops, but can suffer from flow maldistribution when a channel is blocked by a water droplet, while interdigitated channels promote secondary flows through the GDL at the expense of higher pressure drops. As such, the specific flow field geometry being utilized should be considered when trying to understand the desaturation profile of the GDL itself. Although the bulk desaturation of a GDL may appear to be a largely linear process, as seen in Fig. 3-A, when the flow field is spatially segmented into ribs and channels heterogeneous desaturation rates emerge, as seen in Fig. 5, where both the saturation values as well as the desaturation rates are seen to vary. These variations occur between the channel and rib zones, and also on a channel-to-channel and rib-to-rib basis. For example, between channel 3 and channel 4 there is a two-fold difference in the desaturation rate from 15 to 20 min, $0.005\,\mu L\,cm^{-2}\,s^{-1}$ versus $0.003\,\mu L\,cm^{-2}\,s^{-1}$. Additionally, from the spatial saturation maps in Fig. 6, it is seen that large saturation gradients can exist across the domain. As seen in Fig. 7-A, there is a 7% difference in magnitude of the initial saturation between two neighboring segments of the same channel, and their resulting desaturation profiles are different.

Although the initial saturation in this study was not generated by an active PEMFC, previous active fuel cell results show that the current distribution is not homogenous throughout the catalyst layer [39], which would lead to heterogeneous water production across the domain. Depending on the material, this could lead to varying initial conditions and removal characteristics within the porous media. Such current maldistribution has been shown to lead to poor fuel cell performance as well as enhanced degradation of the MEA itself [40]. In a recent study by García-Salaberri et al. [23], it was found that a representative element volume could not be found for a GDL due to the relative thinness of the GDL in relation to the average pore size. Similarly, this study has shown that both desaturation rates and overall saturation can vary across the whole domain. As seen in Fig. 3 and discussed in section 3.1, there was a two-fold difference between transient desaturation rates, thus an overall desaturation rate may not be appropriate when describing this media. As such, as computational power expands PNMs will need to accordingly expand to capture more of the domain in order to further investigate the cause for these observed heterogeneities.

These results also highlight the potential for intelligently engineered materials, which have the potential to replace the anisotropic carbon fiber paper commonly used as the substrate for GDLs. Examples of such designed materials include electrospun GDLs and metallic GDLs. As these more isotropic GDLs are further characterized and investigated, it is possible that the observed spatial gradients between both the overall saturation and desaturation rates will be reduced.

5. Conclusions

The 4-D imaging of the desaturation of an initially flooded GDL by a serpentine flow channel was performed for the first time using synchrotron X-ray CT. Analysis of the overall domain presented a desaturation profile that was comprised of two largely linear regions, with rates ranging between $0.0018 \pm 0.0002\,\mu L\,cm^{-2}\,s^{-1}$ to $0.0042 \pm 0.0004\,\mu L\,cm^{-2}\,s^{-1}$ and an overall rate of $0.0030 \pm 0.0013\,\mu L\,cm^{-2}\,s^{-1}$. As the domain was segmented down to the scale of individual ribs and channels, a heterogeneous distribution of both local saturations and desaturation rates emerged with overall desaturation rates of $0.0034 \pm 0.0012\,\mu L\,cm^{-2}\,s^{-1}$ and $0.0031 \pm 0.0025\,\mu L\,cm^{-2}\,s^{-1}$ for the channel and rib domain respectively. Fully segmented results showed that this heterogeneous behavior was still observed between both neighboring regions and similar geometries. These temporal and spatial gradients show that the initial conditions, intrinsic anisotropy of the material, as well as the local and global geometry of the gas flow field all play a key role in determining the local desaturation behavior of a GDL. Taken together, these results indicate that as computational capabilities expand, larger computational domains will be necessary to accurately represent the multiphase transport within this thin porous media.

Acknowledgements

LFZ and RA acknowledge the support from their respective universities, the University of Saskatchewan and Montana State University. LFZ also acknowledge the financial support from Natural Sciences and Engineering Research Council of Canada. This collaboration was also supported under U.S. NSF Award number 1444198. RA and LB also acknowledge the support from the Center for Biofilm Engineering from Montana State University for access to imaging software. Research described in this paper was performed at the BMIT facility at the Canadian Light Source, which is supported by the Canada Foundation for Innovation, Natural Sciences and Engineering Research Council of Canada, the University of Saskatchewan, the Government of Saskatchewan, Western Economic Diversification Canada, the National Research Council Canada, and the Canadian Institutes of Health Research.

References

[1] Fuel Cell Technologies Office Multi-Year Research, Development, and Demonstration Plan, Department of Energy, 2016, pp. 3.4 1–58.
[2] L. Cindrella, et al., Gas diffusion layer for proton exchange membrane fuel cells—a review, J. Power Sources 194 (1) (2009) 146–160.
[3] J. Bear, Dynamics of Fluids in Porous Media, Courier Corporation, 2013.
[4] C.Z. Qin, S.M. Hassanizadeh, A new approach to modelling water flooding in a polymer electrolyte fuel cell, Int. J. Hydrogen Energy 40 (8) (2015) 3348–3358.
[5] N. Yousfi-Steiner, et al., A review on PEM voltage degradation associated with water management: impacts, influent factors and characterization, J. Power Sources 183 (1) (2008) 260–274.
[6] T. Ous, C. Arcoumanis, Degradation aspects of water formation and transport in proton exchange membrane fuel cell: a review, J. Power Sources 240 (2013) 558–582.
[7] J. Park, et al., A review of the gas diffusion layer in proton exchange membrane fuel cells: durability and degradation, Appl. Energy 155 (2015) 866–880.
[8] F. Lapicque, et al., A critical review on gas diffusion micro and macroporous layers degradations for improved membrane fuel cell durability, J. Power Sources 336 (2016) 40–53.
[9] S. Park, J.-W. Lee, B.N. Popov, A review of gas diffusion layer in PEM fuel cells: materials and designs, Int. J. Hydrogen Energy 37 (7) (2012) 5850–5865.
[10] R. Alink, et al., The influence of porous transport layer modifications on the water management in polymer electrolyte membrane fuel cells, J. Power Sources 233 (2013) 358–368.
[11] H.-H. Chen, M.-H. Chang, Effect of cathode microporous layer composition on proton exchange membrane fuel cell performance under different air inlet relative humidity, J. Power Sources 232 (2013) 306–309.
[12] A. Li, S.H. Chan, Understanding the role of cathode structure and property on water management and electrochemical performance of a PEM fuel cell, Int. J. Hydrogen Energy 38 (27) (2013) 11988–11995.
[13] Y. Wang, et al., Double-layer gas diffusion media for improved water management in polymer electrolyte membrane fuel cells, J. Power Sources 292 (2015) 39–48.
[14] Z. Wang, et al., Improvement of PEMFC water management by employing water transport plate as bipolar plate, Int. J. Hydrogen Energy 42 (34) (2017) 21922–21929.
[15] S. Chevalier, et al., Novel electrospun gas diffusion layers for polymer electrolyte membrane fuel cells: Part II. In operando synchrotron imaging for microscale liquid water transport characterization, J. Power Sources 352 (Supplement C) (2017) 281–290.
[16] B.H. Lim, et al., Effects of flow field design on water management and reactant distribution in PEMFC: a review, Ionics 22 (3) (2016) 301–316.
[17] T.A. Trabold, Minichannels in polymer electrolyte membrane fuel cells, Heat Tran. Eng. 26 (3) (2005) 3–12.
[18] I.S. Hussaini, C.Y. Wang, Dynamic water management of polymer electrolyte membrane fuel cells using intermittent RH control, J. Power Sources 195 (12) (2010) 3822–3829.
[19] C. Damour, et al., A novel non-linear model-based control strategy to improve PEMFC water management – the flatness-based approach, Int. J. Hydrogen Energy 40 (5) (2015) 2371–2376.
[20] L. Battrell, et al., Quantifying cathode water transport via anode relative humidity measurements in a polymer electrolyte membrane fuel cell, Energies 10 (8)

(2017) 16.
[21] H.-W. Wu, A review of recent development: transport and performance modeling of PEM fuel cells, Appl. Energy 165 (2016) 81–106.
[22] M. Andersson, et al., A review of cell-scale multiphase flow modeling, including water management, in polymer electrolyte fuel cells, Appl. Energy 180 (2016) 757–778.
[23] P.A. García-Salaberri, et al., Analysis of representative elementary volume and through-plane regional characteristics of carbon-fiber papers: diffusivity, permeability and electrical/thermal conductivity, Int. J. Heat Mass Tran. 127 (2018) 687–703.
[24] M. Aghighi, J. Gostick, Pore network modeling of phase change in PEM fuel cell fibrous cathode, J. Appl. Electrochem. 47 (12) (2017) 1323–1338.
[25] N. Belgacem, M. Prat, J. Pauchet, Coupled continuum and condensation–evaporation pore network model of the cathode in polymer-electrolyte fuel cell, Int. J. Hydrogen Energy 42 (12) (2017) 8150–8165.
[26] E.F. Medici, et al., Understanding water transport in polymer electrolyte fuel cells using coupled continuum and pore-network models, Fuel Cells 16 (6) (2016) 725–733.
[27] A. Bazylak, Liquid water visualization in PEM fuel cells: a review, Int. J. Hydrogen Energy 34 (9) (2009) 3845–3857.
[28] P. Krüger, et al., Synchrotron X-ray tomography for investigations of water distribution in polymer electrolyte membrane fuel cells, J. Power Sources 196 (12) (2011) 5250–5255.
[29] J. Lee, et al., Synchrotron investigation of microporous layer thickness on liquid water distribution in a PEM fuel cell, J. Electrochem. Soc. 162 (7) (2015) F669–F676.
[30] T. Arlt, et al., Influence of artificially aged gas diffusion layers on the water management of polymer electrolyte membrane fuel cells analyzed with in-operando synchrotron imaging, Energy 118 (2017) 502–511.
[31] D. Muirhead, et al., Liquid water saturation and oxygen transport resistance in polymer electrolyte membrane fuel cell gas diffusion layers, Electrochim. Acta 274 (2018) 250–265.
[32] S. Lal, et al., Determination of water evaporation rates in gas diffusion layers of fuel cells, J. Electrochem. Soc. 165 (9) (2018) F652–F661.
[33] I.V. Zenyuk, et al., Investigating evaporation in gas diffusion layers for fuel cells with X-ray computed tomography, J. Phys. Chem. C 120 (50) (2016) 28701–28711.
[34] L. Battrell, et al., Transient, spatially resolved desaturation of gas diffusion layers measured via synchrotron visualization, Int. J. Hydrogen Energy 43 (24) (2018) 11234–11243.
[35] T.W. Wysokinski, et al., Beamlines of the biomedical imaging and therapy facility at the Canadian light source—Part 1, Nucl. Instrum. Methods Phys. Res. Sect. A Accel. Spectrom. Detect. Assoc. Equip. 582 (1) (2007) 73–76.
[36] Rasband, W.S., *ImageJ*. 1997-2016, U.S. National Institutes of Health: Bethesda, Maryland, USA.
[37] K. Hisatake, et al., Experimental and theoretical study of evaporation of water in a vessel, J. Appl. Phys. 77 (12) (1995) 6664–6674.
[38] Y.V. Lyulin, O.A. Kabov, Measurement of the evaporation mass flow rate in a horizontal liquid layer partly opened into flowing gas, Tech. Phys. Lett. 39 (9) (2013) 795–797.
[39] O.E. Herrera, D.P. Wilkinson, W. Mérida, Anode and cathode overpotentials and temperature profiles in a PEMFC, J. Power Sources 198 (2012) 132–142.
[40] M. Belhadj, et al., Current density distributions in polymer electrolyte fuel cells: a tool for characterisation of gas distribution in the cell and its state of health, Chem. Eng. Sci. 185 (2018) 18–25.